Time-resolved spectroscopy in $LiCaAlF_6$ doped with Cr^{3+}: dynamical Jahn–Teller effect and thermal shifts associated with the $^4T_2$ excited state

2010 J. Phys.: Condens. Matter 22 125502

(http://iopscience.iop.org/0953-8984/22/12/125502)

J. Phys.: Condens. Matter **22** (2010) 125502 (13pp) doi:10.1088/0953-8984/22/12/125502

Time-resolved spectroscopy in $LiCaAlF_6$ doped with Cr^{3+}: dynamical Jahn–Teller effect and thermal shifts associated with the $^4T_2$ excited state

M N Sanz-Ortiz[1], F Rodríguez[1,3] and R Valiente[2]

[1] MALTA CONSOLIDER Team, DCITIMAC, Facultad de Ciencias, Universidad de Cantabria, E-39005 Santander, Spain
[2] MALTA CONSOLIDER Team, Departamento Física Aplicada, Facultad de Ciencias, Universidad de Cantabria, E-39005 Santander, Spain

E-mail: rodriguf@unican.es

Received 17 December 2009, in final form 8 February 2010
Published 8 March 2010
Online at stacks.iop.org/JPhysCM/22/125502

Abstract

This work investigates the centre distribution of the Cr^{3+} impurity, the dynamical Jahn–Teller effect in the first $^4T_2$ excited state and the thermal shifts of the absorption and emission peaks in $LiCaAlF_6$:Cr^{3+} by means of time-resolved emission spectroscopy. The electronic and vibrational fine structure observed in both the absorption and emission spectra at low temperature are assigned according to the vibrational modes of the internal $(CrF_6)^{3-}$ complex and the lattice modes. Zero-phonon lines associated with $^4T_2 \rightarrow {}^4A_2$ and $^2E \rightarrow {}^4A_2$ transitions were detected and assigned on the basis of available high pressure data in $LiCaAlF_6$:Cr^{3+}. We have identified the vibrational coupled modes responsible for the vibrational structure of the low temperature emission spectrum and the reduction of the zero-phonon line (ZPL) splitting caused by the dynamical Jahn–Teller effect in the $^4T_2$ excited state (Huang–Rhys factor, $S_e = 0.92$). In addition, from the temperature variation of the emission intensity $I(T)$, transition energy $E(T)$ and bandwidth $H(T)$, we obtained the vibrational modes that are coupled to the emitting state. We have evaluated the two main contributions to the photoluminescence thermal shift through thermal expansion and high pressure measurements: the implicit contribution induced by changes of thermal population and the explicit contribution induced by thermal expansion effects—40% and 60% of the total shift, respectively.

(Some figures in this article are in colour only in the electronic version)

1. Introduction

Besides applications as tunable solid-state lasers and photoluminescence (PL) materials [1, 2], fluoroelpasolites [3], garnets [4] and niobates [5, 6] are attractive host materials to investigate excited state crossover (ESCO) processes in Cr^{3+} since they provide crystal-field (CF) strengths close to the $^2E \leftrightarrow {}^4T_2$ crossing point (figure 1(a)). In fact, $LiCaAlF_6$:Cr^{3+} provides an ideal CF at the Al site ($\Delta = 1.99$ eV) for investigating ESCO phenomena [7]. In addition, the host material exhibits a first-order structural phase transition (PT) from trigonal ($P\bar{3}1c$: phase I) to monoclinic ($P2_1/c$: phase II) between 7 and 9 GPa [8], which reduces the Cr^{3+} site symmetry, yielding important PL changes [7]. Aside from pressure effects, the optical absorption (OA) and the emission properties of $LiCaAlF_6$:Cr^{3+} show a rather different behaviour with temperature, i.e. the thermal shifts in absorption are practically undetectable whereas the emission band experiences a redshift of about 0.03 eV from 19 to 300 K (figure 2). The fine structure of the low temperature emission spectrum, usually observed in Cr^{3+}-doped fluoroelpasolites [7, 9–15], has been interpreted in terms

[3] Author to whom any correspondence should be addressed.

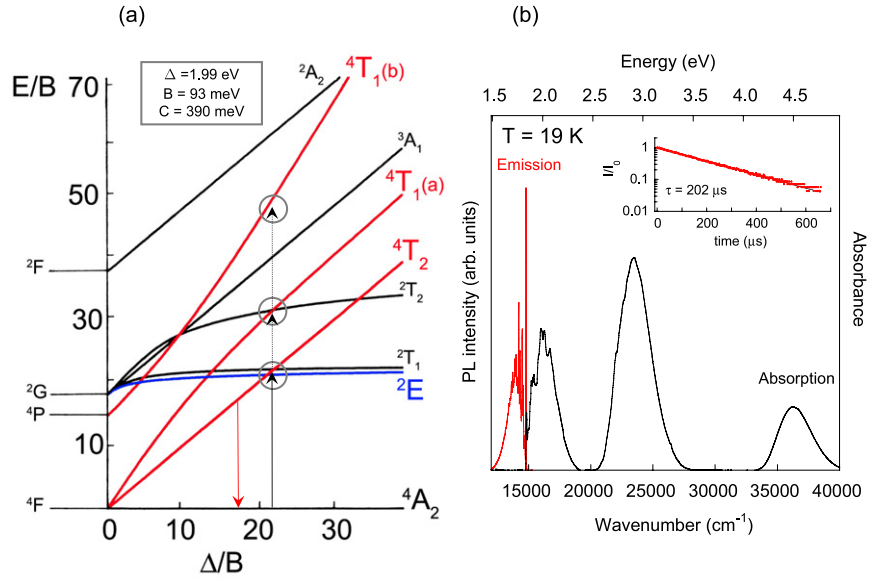

Figure 1. (a) Tanabe–Sugano diagram for d^3 electronic configuration indicating the crystal-field strength of Cr^{3+} in $LiCaAlF_6$. The energies of the room temperature absorption spectrum (circles in the Tanabe–Sugano diagram) correspond to $B = 750\ cm^{-1}$ (93 meV), $C = 3100\ cm^{-1}$ (390 meV) and $\Delta = 16\,080\ cm^{-1}$ (1.99 eV): $C/B = 4.1$; $\Delta/B = 21.4([\Delta/B]_{ESCO} = 22)$. (b) 19 K absorption and PL (excitation wavelength, $\lambda_{exc} = 633$ nm) spectra of $LiCaAlF_6$: 2% Cr^{3+} single crystals. The inset corresponds to the PL decay curve, $I(t)$, with an associated lifetime, $\tau = 202\ \mu s$.

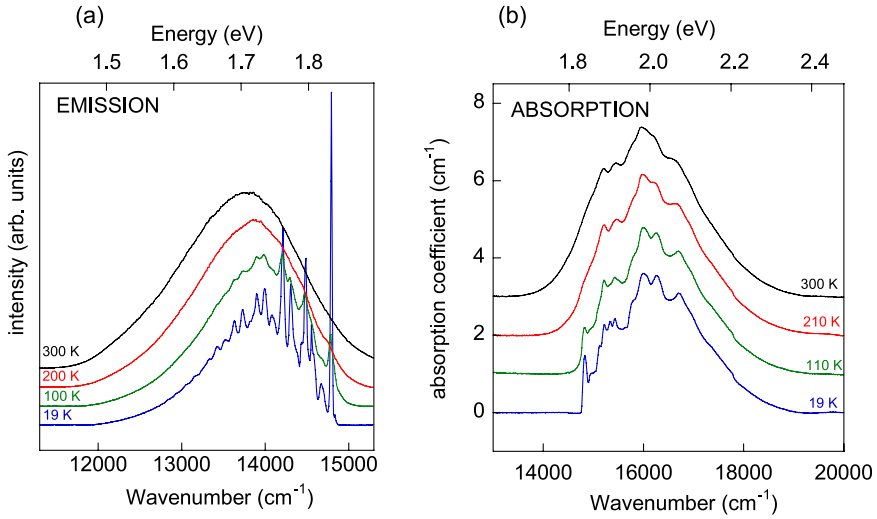

Figure 2. Temperature dependence of the $^4T_2 \rightarrow {}^4A_2$ emission (a) and the $^4A_2 \rightarrow {}^4T_2$ absorption bands (b) of $LiCaAlF_6$:2% Cr^{3+}. The emission spectra were obtained by time-resolved spectroscopy after 50 ns pulsed excitation into the $^4A_2 \rightarrow {}^4T_2$ band using $\lambda = 412$ nm. The counting time was 5 ms. Note the different thermal shift undergone by the emission band in comparison to the absorption band.

of electron–lattice coupling to internal modes of the $(CrF_6)^{3-}$ unit. However, its absorption counterpart structure is not a mirror image of the emission spectra. Actually the low temperature emission spectrum has a simple vibronic side band structure which is mainly constructed from the only spinor populated at low temperature, i.e. the lowest energy one, whereas the absorption band contains a similar vibronic structure but constructed from each one of the spinors arising from the $^4T_2$ manifold. Additionally the absorption fine structure contains fine features associated with the two spin-flip transitions $^4A_2 \rightarrow {}^2E, {}^2T_1$. However, the identification of these narrow features is a difficult task since their associated oscillator strength is weak and both excited states interact with the $^4T_2$ broadband, leading to the characteristic Fano resonances in the absorption spectra [9].

In this work we investigate the emission and absorption spectra as a function of temperature on $LiCaAlF_6$:Cr^{3+} using OA and time-resolved emission spectroscopy techniques, paying attention to the low temperature features. The aim is to understand the asymmetric fine structure observed in the absorption and emission spectra, in terms of electron–phonon coupling and the occurrence of interacting states, as well as the different thermal shifts undergone by the emission and OA bands. Throughout this work we underline the relevance of

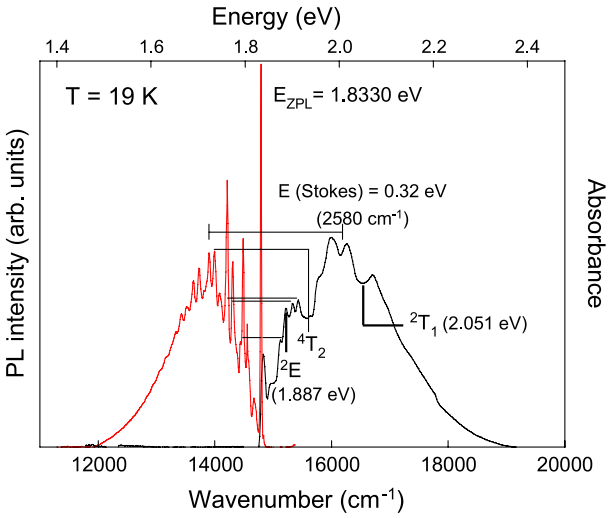

Figure 3. $^4T_2 \rightarrow {}^4A_2$ emission and $^4A_2 \rightarrow {}^4T_2$ absorption bands of $LiCaAlF_6$:2% Cr^{3+} at $T = 19$ K. The bars mark the vibrational energy of the more prominent coupled modes for emission and absorption. The mirror peaks identify the peak associated with vibrational modes in the $^4A_2$ ground state and the $^4T_2$ excited state. Note that the absorption peak at 1.887 eV (^2E) has no twin feature in emission, revealing that it corresponds to the spin-flip electronic transition $^4A_2 \rightarrow {}^2E$. This figure illustrates that the minimum of the emitting $^4T_2$ state is 54 meV below the minimum of the ^2E state or excited state crossover (ESCO). This assignment agrees with that performed on the basis of high pressure measurements elsewhere [7].

an adequate characterization of both Cr^{3+} impurity sites in $LiCaAlF_6$:Cr^{3+} and the knowledge of the vibrational structure in the ground ($^4A_2$) and excited ($^4T_2$) states (mode softening) and the coupling strength for a proper understanding of PL properties with temperature.

2. Experimental details

Time-resolved emission and PL time dependence measurements as a function of temperature were carried out in an $LiCaAlF_6$:Cr^{3+} (2 mol%; $N = [Cr^{3+}] = 1.9 \times 10^{20}$ cm^{-3}) single crystal of laser quality. The time-resolved emission spectra were attained with a Vibrant B 355 II OPO laser using an improved experimental set-up described elsewhere [16, 17]. Absorption spectra were obtained with a Perkin Elmer Lambda 9 spectrophotometer. A closed-cycle He cryostat was employed for measurements in the 19–300 K temperature range using an APD-E controller. The emission spectra were corrected for instrumental response.

3. Results and discussion

3.1. Optical absorption and photoluminescence spectra: crystal-field analysis and variation with temperature

Figure 1(b) shows the 19 K OA and the associated emission spectra of $LiCaAlF_6$:Cr^{3+}. Asides from the rich fine structure associated with the vibrational coupling and the Fano resonances shown by the first excited state $^4T_2$ (octahedral

Table 1. Transition energies and associated Racah (B, C) and CF splitting (Δ) parameters of Cr^{3+} in $LiCaAlF_6$:Cr^{3+}, obtained from the OA spectrum at 300 and 19 K through moment analysis.

Temperature (K)	Absorption (eV) $^4A_2 \rightarrow$ $^4T_2$	$^4T_1$ (a)	$^4T_1$ (b)	Δ (eV)	B (meV)	C (meV)	C/B
300	1.99	2.90	4.48	1.99	93	390	4.2
19	2.03	2.93	4.53	2.03			

symmetry notation), the three absorption bands at 2.03, 2.93 and 4.53 eV correspond to CF transitions within the $3d^3$ configuration of Cr^{3+} from the $^4A_2$ ground state to $^4T_2$, $^4T_1$ (a) and $^4T_1$ (b) excited states, respectively. The CF parameters of Cr^{3+} in $LiCaAlF_6$:Cr^{3+}, obtained from its OA spectrum at 300 K and its location in the Tanabe–Sugano diagram (figure 1(a)), make it attractive for inducing Cr^{3+} ESCO through high pressure [7, 18]. The transition energies and the associated Racah parameters (B, C) and CF splitting parameter (Δ) are collected in table 1. Figure 2 shows the OA and PL spectra of $LiCaAlF_6$:Cr^{3+} as a function of the temperature in the 19–300 K range. Note that the centroid of the PL band blueshifts when reducing temperature from 300 K to 19 K, being located at 1.70 eV and 1.73 eV, respectively. This feature is a consequence of the positive slope (or CF dependence) of the $^4T_2$ state; actually the $^4A_2 \rightarrow {}^4T_2$ transition energy directly gives the parameter Δ. This emission blueshift of 30 meV is practically undetectable in absorption, the centroid of which is about 2.0 eV (figure 2). As we will show later, the odd-parity assistance mechanism and the vibration mode softening in the $^4T_2$ excited state are both responsible for the different thermal shifts of the emission and absorption bands.

It is worth noting how the fine structure exhibited by the $^4T_2 \rightarrow {}^4A_2$ emission band is much better resolved than the corresponding $^4A_2 \rightarrow {}^4T_2$ absorption band. Most peaks in emission correspond to vibrational coupling with the $^4T_2$ state constructed from the ZPL at 1.833 eV at 19 K, whereas the absorption side band consists of a similar vibronic pattern but constructed from each of the ZPLs: $^4A_2 \leftrightarrow {}^4T_2 + {}^2E + {}^2T_1$. In addition, sharp features associated with the contributions from the $^4A_2 \rightarrow {}^2E$ transition are also present, making the peak structure of the first absorption band more complex and less resolved than the emission band.

Figure 3 shows the fine structure in absorption and emission at 19 K. An important difference between these spectra is the presence of three prominent peaks in absorption located 50 meV above the ZPL energies, at 1.887, 1.902 and 1.913 eV. The former should have a similar mirror peak in emission around 1.78 eV but, in fact, no spectral feature is detected in emission in such a spectral region. On the basis of pressure-induced excited state crossover ($^2E \leftrightarrow {}^4T_2$), this first absorption peak at 1.887 eV corresponds to the Fano resonance of the ^2E state and hence its maximum directly provides the energy of the ^2E state (figure 3), following the peak assignment given elsewhere [9]. The two other absorption peaks may be either: (1) vibronic replicas from ^2E of 15 and 26 meV, respectively, according to an interpretation

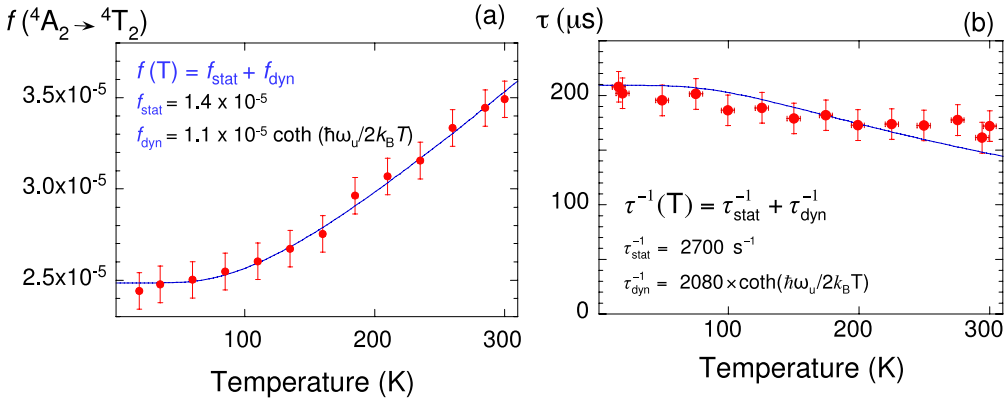

Figure 4. (a) Temperature dependence of the oscillator strength $f(T)$ obtained from the zero-order moment of the $^4A_2 \rightarrow {}^4T_2$ absorption band of $LiCaAlF_6$:2% Cr^{3+} and (b) the reciprocal lifetime $\tau^{-1}(T)$. The oscillator strength $f(T)$ was obtained from the absorption integrated intensity (zero-order moment) $M_0(T) = \int_{\text{Band}} k(\text{cm}^{-1})\,\text{d}E$ (eV) through equation (5), using a refractive index of $n = 1.92$ [35], $N = [Cr^{3+}] = 1.9 \times 10^{20}$ cm^{-3}. The curves correspond to the fit of the experimental data to equation (3). The enabling-coupled vibrations are the odd-parity modes t_{2u} (28.8 meV, 232 cm^{-1}) and t_{1u} (s) (72.0 meV, 581 cm^{-1}), with $f(t_{2u}) = 1.1 \times 10^{-5}$ and $f(t_{1u}(s)) = 1.4 \times 10^{-5}$. (b) Experimental lifetime variation with temperature $\tau(T)$ and the corresponding fit to equation (1). The fitting parameters are: $\tau^{-1}_{\text{stat}} = 2700$ s^{-1} and $\tau^{-1}_{\text{dyn}} = 2080$ s^{-1} at 0 K and $\hbar\omega_u(t_{2u}) = 28.8$ meV keeping the $\frac{\tau^{-1}_{\text{stat}}}{\tau^{-1}_{\text{dyn}}}$ ratio as $\frac{f_{\text{stat}}}{f_{\text{dyn}}} = 1.3$.

given elsewhere [9, 19] or (2) vibrational replicas from the ZPL associated with the t_{2g} and e_g modes given that similar replicas are observed in the emission spectrum (figure 3). Accordingly, the dip-shaped structure at 2.051 eV would correspond to the $^2T_1$ Fano anti-resonance [9, 18]. With the present assignment we are able to explain why $LiCaAlF_6$:Cr^{3+} exhibits a broadband PL instead of ruby-like narrow line emission, bearing in mind that the $LiCaAlF_6$ host provides the highest CF strength ($\Delta = 1.99$ eV) among fluorides [9]. In fact, narrow line emission from ^2E in Cr^{3+} at low temperature takes place once the ^2E ZPL energy lies below the $^4T_2$ ZPL energy: the excited state crossover (ESCO) condition, i.e. the energy difference $\delta E_{\text{ZPL}} = E_{\text{ZPL}}(^4T_2) - E_{\text{ZPL}}(^2E) > 0$. As derived from figure 3, $\delta E_{\text{ZPL}} = -54$ meV in $LiCaAlF_6$:Cr^{3+} at 19 K and thus a broadband emission from $^4T_2$ dominates the PL spectrum at low and high temperatures and ambient pressure. High pressure conditions can lead to $^4T_2 \leftrightarrow {}^2E$ crossover and thus transform the PL behaviour of Cr^{3+} from broadband emission to narrow line PL [7, 18]. Actually, high pressure experiments in K_2NaGaF_6:Cr^{3+} [3], Rb_2KCrF_6 [9] and $LiCaAlF_6$:Cr^{3+} [7] have shown the usefulness of this technique to achieve such a transformation from pressures above 5 GPa. Estimates based on the pressure shifts of $^4T_2$ and ^2E states measured in $LiCaAlF_6$:Cr^{3+} (11.0 meV GPa^{-1} for $^4T_2$ and -0.4 meV GPa^{-1} for ^2E) agree with this value [18]. It must be noted that the actual pressure to get R-line emission from Cr^{3+} at room temperature is 28 GPa. These extreme high pressure conditions are required to mostly populate the ^2E state ($\tau = 2.7$ ms) avoiding the thermal population of the shorter-lifetime $^4T_2$ state ($\tau = 202$ μs) [18].

The reciprocal lifetime increases with temperature following a characteristic hyperbolic cotangent function plus a constant term which are referred to as static and dynamic terms [1]:

$$\begin{aligned} \tau^{-1}(T) &= \tau^{-1}_{\text{stat}}(T) + \tau^{-1}_{\text{dyn}}(T) \\ \tau^{-1}_{\text{stat}}(T) &= \tau^{-1}_{\text{MD}}(T) + \tau^{-1}_{\text{ED}}(T) \\ \tau^{-1}_{\text{dyn}}(T) &= \sum_i \tau^{-1}_{0i} \coth\left[\frac{\hbar\omega_{ui}}{2k_{\text{B}}T}\right]. \end{aligned} \tag{1}$$

The first term refers to the transition probability due to the magnetic-dipole ($\tau^{-1}_{\text{MD}}(T)$) as well as electric-dipole (ED) mechanisms induced by non-centrosymmetric CF distortions at the Cr^{3+} site ($\tau^{-1}_{\text{ED}}(T)$) and is independent, or slightly dependent, on temperature, whereas the second term is ED-assisted by ith odd-parity vibrations of energy $\hbar\omega_{ui}$. The latter mainly governs the temperature dependence $\tau(T)$, which shape gives the energy and the relative oscillator strength of each coupled vibration. It is important to note that a similar thermal dependence is found for the integrated intensity of the first absorption band $I(T)$, i.e. the zero-order moment of the absorption band, $M_0(T)$. Its analysis is shown in figure 4.

3.2. Time-resolved spectroscopy in the $^4T_2$ excited state. Excited state dynamics and Jahn–Teller effect

Interestingly, the $^4T_2$ ZPL at 1.833 eV shows the fine structure due to the spin–orbit interaction within the $^4T_2$ manifold (figures 5 and 6). Not all seven lines observed in the absorption spectrum at 19 K (figure 5) are associated with the same $(CrF_6)^{3-}$ centre, as was already reported [1]. The thermal dependence of each of these components in the PL spectrum and their associated lifetimes show that A_1 (1.8330 eV), A_2 (1.8347 eV), A_3 (1.8390 eV) and A_4 (1.8409 eV) ($=\Gamma_7, \Gamma_8, \Gamma'_8, \Gamma_6$) lines correspond to the $^4T_2$ manifold spinors of the dominant $(CrF_6)^{3-}$ centre ($\tau = 202$ μs) whereas C_1, D_1 and E_1 have significantly different lifetimes and probably belong to other minor centres or aggregates. By just considering the spin–orbit interaction on

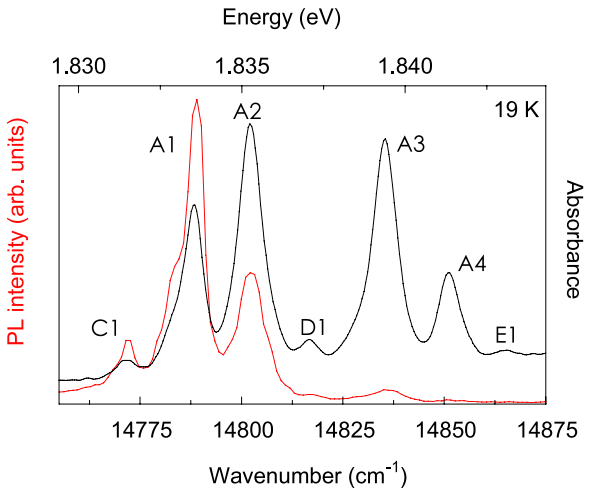

Figure 5. 19 K absorption and emission spectra (excitation wavelength, $\lambda_{exc} = 633$ nm) at 19 K of $LiCaAlF_6$:2% Cr^{3+} around the zero-phonon line. The four spinors $A_1(\Gamma_7)$, $A_2(\Gamma_8)$, $A_3(\Gamma'_8)$ and $A_4(\Gamma_6)$ peak at 14 784 cm^{-1} (1.8330 eV), 14 798 cm^{-1} (1.8347 eV), 14 832 cm^{-1} (1.8390 eV) and 14 848 cm^{-1} (1.8409 eV), respectively.

the $^4T_2$ state the ZPL splitting should be around 150 meV considering a spin–orbit coupling constant $\zeta = 226$ cm^{-1} (figure 7). The smaller ZPL splitting experimentally measured reveals the occurrence of a dynamical Jahn–Teller effect (JTE) on the $^4T_2$ state [20]. Similar effects have been observed in other Cr^{3+}-doped fluorides [9–15] and chlorides [21], and in Mn^{2+}-doped fluorides [22]. The present spinor assignment, which is based on the relative spinor intensity observed in absorption, is different to that given elsewhere [23], in which the ZPLs were assigned to Γ_7, Γ_8, Γ_6 and Γ'_8 (figure 6(c)), respectively.

The temperature variation of the relative intensity $I_{A_i}(T)$, $i = 1$–4, of the ZPL emission components (figure 6(a)) follows the Boltzmann population according to the energy separation of the spinors in the $^4T_2$ excited state as is shown in figure 6(b). Solid lines correspond to the calculated emission intensities using the ZPL energies and intensities derived from the absorption spectrum. It must be noted that the absence of a PT upon cooling at ambient pressure is advantageous for a clear observation of the ZPL structure in the low temperature PL spectrum, which is not the case in other Cr^{3+}-doped fluoroelpasolites due to explosive PT occurrence [24, 25].

As was previously mentioned, the $^4T_2$ splitting into four spinors is smaller than the calculated splitting on the basis of the spin–orbit constant of the free Cr^{3+} ion. This phenomenon, which is usually observed in TM ions having an orbitally degenerate PL excited state as Cr^{3+} [20, 21, 26–28] or Mn^{2+} [22], is due to the Ham reduction caused by the dynamical JTE in the $^4T_2$ manifold state [29]. These degenerate states are unstable to certain low symmetry (tetragonal and rhombic symmetry) CF distortion and are thus subjected to the JTE [30]: electron–phonon coupling of the octahedral $^4T_2$ state with e_g or t_{2g} vibrations. Within the JT theory it is well established that the expected value of any orbital operator for the vibronic wavefunctions of the twelvefold-degenerate $^4T_2$ state is reduced by the overlap of the vibrational wavefunctions. In fact, if we denote the $^4T_2$ vibronic wavefunctions by $|\Psi(^4T_2, i, j); \Phi_{vib}(Q_\theta, Q_\varepsilon)\rangle$,

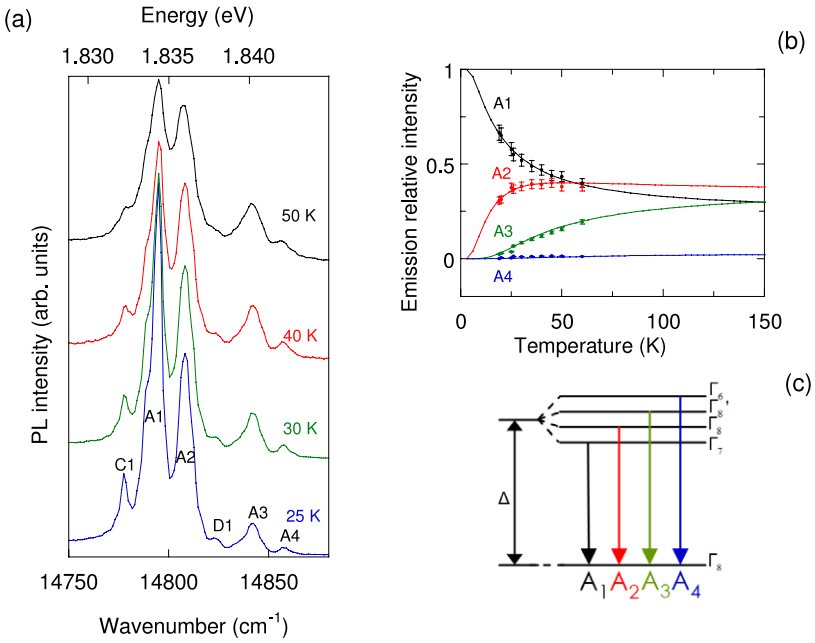

Figure 6. Variation of the zero-phonon line emission spectra with temperature in the 25–50 K range. (b) Variation of the relative A_i emission intensity, $f_j = \frac{I_j}{\sum_i I_i} = \frac{f_{os,i}}{\sum_i f_{os,i}}$, with temperature and calculated values using the relative oscillator strengths derived from the low temperature absorption spectrum: $f(A_1) = 0.21$, $f(A_2) = 0.36$, $f(A_3) = 0.34$ and $f(A_4) = 0.09$. The population of each spinor is given by the Boltzmann distribution: $I_j = \frac{(f_j/d_j)d_j e^{-E(A_j)/K_B T}}{Z} = \frac{f_j e^{-E(A_j)/K_B T}}{Z}$ with $Z = 1 + 2e^{-E(A_2)/K_B T} + 2e^{-E(A_3)/K_B T} + e^{-E(A_4)/K_B T}$. The fitted f_j values are: $f(A_1) = 0.14$, $f(A_2) = 0.40$, $f(A_3) = 0.44$ and $f(A_4) = 0.02$. Note the fair agreement between the fitted f_j values and those directly derived from the absorption spectrum. (c) Scheme of the four spin–orbit components of the $^4T_2$ state.

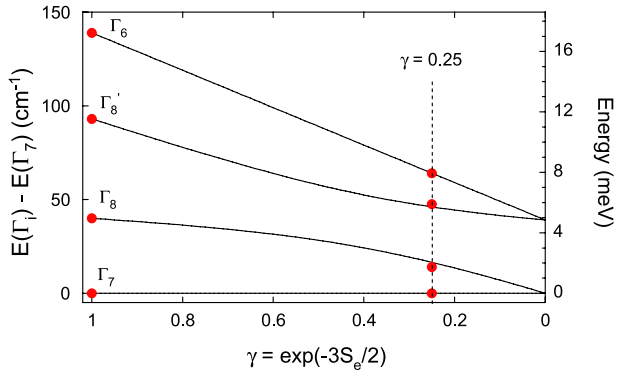

Figure 7. Relative energy of the four spin–orbit components of the $^4T_2$ state in $LiCaAlF_6$:Cr^{3+} in O′-double-group irreducible representation. The points corresponding to $\gamma = 1$ have been calculated using the full d^3 matrix [13, 14] with the following parameters (all in cm^{-1}): $\Delta = 1450$ cm^{-1}, $B = 760$ cm^{-1}, $C = 3430$ cm^{-1} and $\zeta_{SO} = 226$ cm^{-1}. The calculated energies referred to the Γ_7 spinor are $E(\Gamma_7) = 0$, $E(\Gamma_8) = 40$ cm^{-1}; $E(\Gamma_8') = 93$ cm^{-1}; $E(\Gamma_6) = 139$ cm^{-1}, the corresponding fit to the effective Hamiltonian parameters being $\lambda = 29.8$ cm^{-1}; $\kappa = 9.65$ cm^{-1}; $\rho = -29.2$ cm^{-1}; the curves correspond to the spinor energy $E(\Gamma_i) - E(\Gamma_7)$ for $i = 6$, 8 and 8′ as a function of the Ham parameter $\gamma = \exp(-3E_{JT}/2\hbar\omega_e)$ according to equation (2). The points depicted at $\gamma = 0.25$ correspond to the experimental ZPL energies relatives to the lowest energy spinor $E(\Gamma_7) = 1.8330$ eV (figures 5 and 6) [23]. The experimental and calculated energies including the Jahn–Teller effect with the Ham parameter $\gamma = 0.25$ are (in cm^{-1}):

	$E(\Gamma_7)$	$E(\Gamma_8)$	$E(\Gamma_8')$	$E(\Gamma_6)$
Expt:	0	14	48	64
Calc:	0	16	46	64

where Ψ refers to the electronic wavefunction with i ($=x, y, z$) and j ($=-3/2 \cdots 3/2$) being the orbital and spin quantum numbers, and Φ_{vib} the corresponding vibrational wavefunction centred at the $Q_i = (Q_{\theta i}, Q_{\varepsilon i})$ point (i: u, v, w) of the three minima of the configurational energy curve of the $^4T_2$ excited state in Q_e-space ($T \otimes e$ JTE) [31], then the matrix element of the spin–orbit interaction Hamiltonian involving the orbital operator L is modulated by the vibrational overlap between different electronic states as

$$\begin{aligned}
&\langle \Psi(^4T_2, i, j); \Phi_{vib}(Q_u)|H_{SO}|\Psi(^4T_2, k, l); \Phi_{vib}(Q_v)\rangle \\
&\quad = \langle \Psi(^4T_2, i, j)|H_{SO}|\Psi(^4T_2, k, l)\rangle\langle \Phi_{vib}(Q_u)|\Phi_{vib}(Q_v)\rangle \\
&\quad = \langle H_{SO}\rangle \left[\delta_{u,v} + (1 - \delta_{u,v})e^{\frac{-3}{2}\frac{E_{JT}}{\hbar\omega_e}}\right] \\
&\quad = \langle H_{SO}\rangle \left[\delta_{u,v} + (1 - \delta_{u,v})e^{\frac{-3}{2}S_e}\right]
\end{aligned}$$

where H_{SO} is the effective spin–orbit Hamiltonian within $^4T_2$:

$$H_{SO} = \lambda L \cdot S + k(L \cdot S)^2 + \rho(L_x^2 S_x^2 + L_y^2 S_y^2 + L_z^2 S_z^2)$$

with $L = 1$ and $S = 3/2$ representing the effective angular momentum operator and the total spin operator within $^4T_2$, E_{JT} the JT energy and S_e the Huang–Rhys factor associated with the JT active e_g vibration. The reduction factor, $\gamma = e^{-1.5S_e}$, known as the Ham reduction [29], is $\gamma = 0.13$ in $(CrCl_6)^{3-}$ formed in chloroelpasolites [21], which implies a Huang–Rhys factor of $S_e = 1.4$. This reduction is about 0.3 ($S_e = 0.8$) in $(CrF_6)^{3-}$ in fluoroelpasolites [20]. This means that the spin–orbit interaction, and hence the ZPL splitting, is reduced by about 10% by the dynamical JT effect. The analytical expressions of the Γ_i spinor energy have been derived by Brik *et al* [20, 26] by diagonalizing the full 12×12 spin–orbit Hamiltonian matrix within $^4T_2$. The spinors energies are given by

$$\begin{aligned}
E(\Gamma_6) &= \tfrac{3}{2}\lambda\gamma + \tfrac{9}{4}k\gamma + \tfrac{7}{2}(k + \rho - k\gamma) \\
E(\Gamma_7) &= \tfrac{-5}{2}\lambda\gamma + \tfrac{25}{4}k\gamma + \tfrac{7}{2}(k + \rho - k\gamma) \\
E(\Gamma_8)_{1,2} &= \frac{A + B}{2} \pm \sqrt{\frac{1}{4}(A - B)^2 + \frac{9}{25}(k + \rho - k\gamma)^2}
\end{aligned} \tag{2}$$

with $A = -\lambda\gamma + k\gamma + \frac{17}{10}(k + \rho - k\gamma)$ and $B = \frac{3}{2}\lambda\gamma + \frac{9}{4}k\gamma + \frac{33}{10}(k + \rho - k\gamma)$.

The observed ZPL structure of the $^4T_2$ state corresponds to the four spinors $\Gamma_7, \Gamma_8, \Gamma_8', \Gamma_6$ (O′ double-group irrep notation). As can be seen in figure 7, the $^4T_2$ experimental ZPL splitting is smaller than the calculated one using the spectroscopic parameters derived from the absorption spectra of $LiCaAlF_6$:Cr^{3+} and spin–orbit constant of $\zeta = 226$ cm^{-1} [26]. Using equation (2), we obtain a Ham reduction of $\gamma = 0.25$ for $LiCaAlF_6$:Cr^{3+}. This means that the Huang–Rhys parameter associated with e_g is $S_e = 0.92$. From the e_g mode frequency ($\hbar\omega_e = 60.9$ meV; 491 cm^{-1}), we derived the JT energy as: $E_{JT} = 56.0$ meV (452 cm^{-1}). This JT energy is significantly higher than that obtained for $CrCl_6^{3-}$ complexes, $E_{JT} = 39$ meV (312 cm^{-1}) [21], and contrasts with those obtained for other $(CrF_6)^{3-}$ complexes spreading over as $E_{JT} = 44$ meV (356 cm^{-1}) ($KMgF_3$ [26]), $E_{JT} = 35$ meV (282 cm^{-1}) (Cs_2NaScF_6 [14]) and $E_{JT} = 31$ meV (250 cm^{-1}) (Cs_2NaYF_6 [15]) (see table 2). The observed trend in fluorides reveals that, like E_{JT}, S_e increases with decreasing metal–fluorine distance (R_{M-F}) of the host crystal. This effect must be mainly ascribed to the weakening of the JT-related electron–phonon coupling upon increasing R_{M-F}. Therefore the Ham effect is more efficient in fluorides providing shorter R_{M-F} to accommodate Cr^{3+}, hence the spin–orbit reduction appears enhanced at smaller volume host sites.

3.3. Vibrational structure in absorption and emission: electronic origins and mode assignment

The absorption and its corresponding emission spectra at 19 K are shown in figure 3. It must be noted that the vibrational features exhibited by both spectra are not mirror images from the ZPL. This behaviour is due to (1) the slightly different vibrational energy ($\hbar\omega_i$) and the related electron–phonon couplings (S_i) of the excited ($^4T_2$) and the ground ($^4A_2$) states; (2) the phonon side band of the low temperature emission spectrum is simpler than the absorption vibrational one since the former is constructed from the Γ_7 spinor alone whereas the four sets of spinors contribute to the phonon side band in the latter and (3) apart from the JT coupling in the $^4T_2$ state, the absorption side band involves transitions from $^4A_2$ to ^2E and $^2T_1$ states, making this band more complex than the emission one. Figure 8 includes the peak labelling of the emission spectrum, the assignment of which is collected in

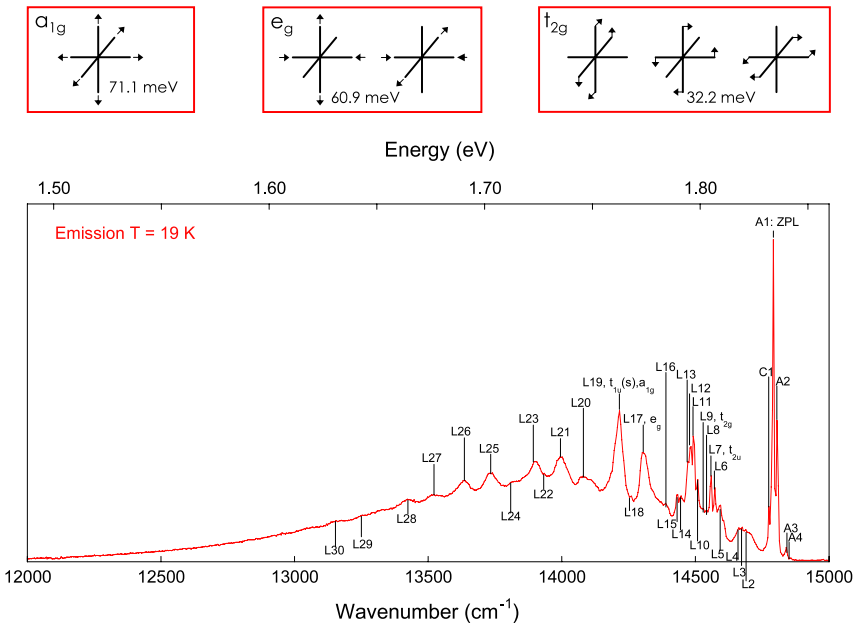

Figure 8. 19 K emission spectrum of $LiCaAlF_6$:2% Cr^{3+}. The vibronic fine structure unravels coupling to different internal modes of $(CrF_6)^{3-}$. The assignment of $L\alpha$ ($\alpha = 1$–31) lines to vibrational replicas from the ZPL is given in table 3. The most relevant vibrations associated with coupled modes in the $(CrF_6)^{3-}$ centre (O_h symmetry) are shown at the top of the figure.

Table 2. Zero-phonon line energy (E_{ZPL}), vibrational energy of a_{1g} and e_g modes, Jahn–Teller energy (E_{JT}), Ham reduction parameter (γ) and corresponding Huang–Rhys parameter (S_e), and M–F and Cr–F bond distances for different Cr^{3+}-doped and Cr^{3+}-pure fluorides. The metal–ligand bond distances were obtained from x-ray diffraction for M–F (R_{M-F}) and the local a_{1g} mode frequency for Cr–F (R_{Cr-F}) following the procedure established elsewhere [9]: $R_{Cr-F} = 3.7305(\hbar\omega_{a_{1g}})^{-0.16}$. The exponent ($-0.16$) corresponds to a local Grüneisen parameter of $\gamma_{loc}(a_{1g}) = 2.1$.

		$\hbar\omega$ (meV)					R (Å)		
Cr^{3+} host	E_{ZPL} (eV)	a_{1g}	e_g	E_{JT} (meV)	γ	$S(e_g)$	M–F	Cr–F	Reference
K_2NaAlF_6:Cr^{3+}	1.877	71.3	61.2				1.806	1.895	[9, 13, 37]
$LiCaAlF_6$:Cr^{3+}	1.833	71.1	60.9	56	0.25	0.92	1.806	1.896	Present work
K_2NaCrF_6		70.7					1.897	1.897	[9]
K_2NaGaF_6:Cr^{3+}	1.865	70.4	59.6				1.874	1.899	[9, 11, 13]
$KMgF_3$:Cr^{3+}	1.798	69.7	56.7	44	0.31	0.78		1.902	[26, 38]
Rb_2KGaF_6:Cr^{3+}	1.783	68.9	58.0				1.892	1.905	[9–11, 27]
Rb_2KCrF_6		67.6					1.90	1.912	[9, 27]
K_2NaScF_6:Cr^{3+}	1.771	67.2	55.7				1.984	1.913	[9, 11, 12, 39]
Tl_2KCrF_6	1.759	66.5					1.92	1.92	[9, 11]
Rb_2NaYF_6:Cr^{3+}	1.755						2.17	1.923	[10, 40]
Rb_2KInF_6:Cr^{3+}	1.764						2.02		[9, 11]
Cs_2NaScF_6:Cr^{3+}	1.720	62.7	50.2	35	0.35	0.70	2.041	1.934	[10, 14, 41]
Cs_2NaYF_6:Cr^{3+}	1.713	62.1	49.8	31	0.39	0.63	2.27	1.937	[10, 15, 42]

table 3. The fine structure assignment was performed on the basis of electron–phonon coupling to different combinations of vibrational quanta of the $(CrF_6)^{3-}$ centre in $LiCaAlF_6$. The peak energy of each vibronic peak is given by $E(L_i) = E_{ZPL} + \sum n_j \hbar\omega_j$, where j refers to the jth coupled mode and n_j the corresponding number of coupled quanta. Table 3 also includes the calculated energy of the 31 observed vibronic peaks using the $(CrF_6)^{3-}$ vibrational mode energies given in table 3. The one-phonon emission spectrum (figure 9) gives us a first sight of the electron–phonon coupling of each mode through their relative intensity with respect to the ZPL intensity, i.e. the Huang–Rhys factor $S_i = \frac{I_i}{I_{ZPL}}$, for each ith coupled mode. The Huang–Rhys factors have been obtained by

$$\frac{I(a_{1g}, t_{1u(s)})}{I_{ZPL}} = S_{a_{1g}} + S_{t_{1u(s)}} = 1.2 \qquad \frac{I(e_g)}{I_{ZPL}} \approx S_e = 0.9$$

$$\frac{I(t_{2u(b)})}{I_{ZPL}} = 0.5.$$

It is worth noting the tight correlation between the R_{M-F} and the frequencies of the stretching modes a_{1g} and e_g, which are known to increase with decreasing R_{M-F}. Following the procedure employed elsewhere [9], the totally symmetric mode a_{1g} of $(CrF_6)^{3-}$ can be used as a probe for deriving the local Cr–F distance (R_{Cr-F}) in Cr^{3+}-doped fluoroelpasolites after correlations established elsewhere [9, 10]. The so-derived

Table 3. Peak positions (energies) of the ZPLs and corresponding vibrational features of the emission band at 19 K. Peak labelling is the same as used in figure 8. The peak assignment is done on the basis of ZPL, vibrations and number of quanta of the coupled modes. The experimental peak positions and energies were corrected for the refractive index of the air ($1/\lambda_{vac} = 1/n_{air}\lambda_{air}$) using $n_{air} = 1.000\,27$. The energy of the vibrational modes of the octahedral complex $(CrF_6)^{3-}$ formed in $LiCaAlF_6{:}Cr^{3+}$ was obtained by fitting the calculated energies to the experimental peak positions.

	Vibration	a_{1g}	e_g	t_{2g}	t_{2u}	t_{1u} (b)	t_{1u} (s)
	$\hbar\omega$ (meV)	71.1 ± 0.1	60.9 ± 0.1	32.2 ± 0.1	28.8 ± 0.1	38.6 ± 0.1	72.0 ± 0.1
	(cm^{-1})	(573 ± 1)	(491 ± 1)	(260 ± 1)	(232 ± 1)	(311 ± 1)	(581 ± 1)
Peak	Position (cm^{-1})	From ZPL (cm^{-1})	Calculated (cm^{-1})	Assignment	E_{exp} (eV)	$E_{ZPL} - E_{exp}$ (meV)	$E_{ZPL} - E_{calc}$ (meV)
	14 848	64	64	A4	1.8409	7.9	7.9
	14 832	48	48	A3	1.8390	6.0	6.0
	14 798	14	14	A2	1.8347	1.7	1.7
L0	14 784	0	0	A1, 0 ZPL	1.8330	0.0	0.0
L1	14 766	−18	−18	C1, other	1.8308	−2.2	−2.2
L2	14 681	−103	−103		1.8202	−12.8	−12.8
L3	14 670	−114	−114	Lattice modes (r)	1.8189	−14.1	−14.1
L4	14 653	−131	−131		1.8168	−16.2	−16.2
L5	14 586	−198	−196	t_{2g} − A4	1.8085	−24.5	−24.3
L6	14 563	−221	−218	t_{2u} − A2	1.8056	−27.4	−27.0
L7	14 552	−232	−232	t_{2u}	1.8042	−28.8	−28.8
L8	14 535	−249	−246	t_{2g} − A2	1.8021	−30.9	−30.5
L9	14 524	−260	−260	t_{2g}	1.8008	−32.2	−32.2
L10	14 501	−283	−280	t_{2u} − A3	1.7979	−35.1	−34.7
L11	14 484	−300	−297	t_{1u}(b) − A2	1.7958	−37.2	−36.8
L12	14 473	−311	−311	t_{1u} (b)	1.7944	−38.6	−38.6
L13	14 462	−322	−329	t_{1u}(b) + C1	1.7931	−39.9	−40.8
L14	14 434	−350	—	—	1.7896	−43.4	—
L15	14 423	−361	−359	t_{1u}(b) − A3	1.7882	−44.8	−44.5
L16	14 377	−407	—	—	1.7825	−50.5	—
L17	14 293	−491	−491	e_g	1.7721	−60.9	−60.9
L17	14 293	−491	−492	$t_{2g} + t_{2u}$	1.7721	−60.9	−61.0
L18	14 254	−530	−520	$2t_{2g}$	1.7673	−65.7	−64.4
L19	14 218	−573 (elbow)	−573	a_{1g}	1.7628	−71.1	−71.1
L19	14 203	−581	−581	t_{1u} (s)	1.7610	−72.0	−72.0
L20	14 074	−710	−723	$e_g + t_{2u}$	1.7450	−88.0	−86.4
L21	13 989	−795	−780	$3t_{2g}$	1.7344	−98.6	−96.7
L21	13 989	−795	−805	$a_{1g} + t_{2u}$	1.7344	−98.6	−99.8
L21	13 989	−795	−802	$e_g + t_{1u}$ (b)	1.7344	−98.6	−99.4
L22	13 927	−857	—	—	1.7267	−106.3	—
L23	13 888	−896	−884	$a_{1g} + t_{1u}$ (b)	1.7219	−111.1	−109.6
L24	13 803	−981	−982	$2e_g$	1.7114	121.8	−121.8
L24	13 803	−981	−983	$e_g + t_{2g} + t_{2u}$	1.7114	121.8	−121.9
L25	13 725	−1059	−1065	$a_{1g} + t_{2g} + t_{2u}$	1.7017	−131.3	−132.0
L25	13 725	−1059	−1064	$a_{1g} + e_g$	1.7017	−131.3	−131.9
L25	13 725	−1059	−1062	$e_g + t_{2g} + t_{1u}$ (b)	1.7017	−131.3	−131.7
L25	13 725	−1059	−1072	$e_g + t_{1u}$ (s)	1.7017	−131.3	−132.9
L26	13 629	−1155	−1154	$a_{1g} + t_{1u}$ (s)	1.6898	−143.2	−143.1
L26	13 629	−1155	−1146	$2a_{1g}$	1.6898	−143.2	−142.1
L27	13 511	−1273	−1271	$e_g + 3t_{2g}$	1.6752	−157.8	−157.6
L27	13 511	−1273	−1272	$4t_{2g} + t_{2u}$	1.6752	−157.8	−157.7
L27	13 511	−1273	−1293	$a_{1g} + 2t_{2g}$	1.6752	−157.8	−160.3
L27	13 511	−1273	−1296	$a_{1g} + e_g + t_{2u}$	1.6752	−157.8	−160.7
L27	13 511	−1273	−1293	$2e_g + t_{1u}$ (b)	1.6752	−157.8	−160.3
L28	13 415	−1369	−1375	$a_{1g} + e_g + t_{1u}$ (b)	1.6633	−169.7	−170.5
L28	13 415	−1369	−1378	$2a_{1g} + t_{2u}$	1.6633	−169.7	−170.9
L28	13 415	−1369	−1361	$3t_{2g} + t_{1u}$ (s)	1.6633	−169.7	−168.7
L29	13 241	−1543	−1555	$a_{1g} + 2e_g$	1.6417	−191.3	−192.8
L29	13 241	−1543	−1563	$2e_g + t_{1u}$ (s)	1.6417	−191.3	−193.8
L30	13 145	−1639	−1645	$a_{1g} + e_g + t_{1u}$ (s)	1.6298	−203.2	−204.0
L30	13 145	−1639	−1637	$2a_{1g} + e_g$	1.6298	−203.2	−203.0
L30	13 145	−1639	−1621	$4t_{2g} + t_{1u}$ (s)	1.6298	−203.2	−201.0
L31	13 145	−1639	−1719	$3a_{1g}$	1.6298	−203.2	−213.1

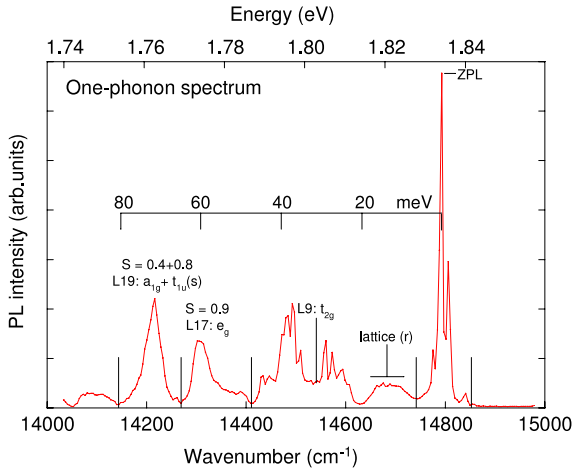

Figure 9. One-phonon replica from the ZPL ($E = 1.8330$ eV) of $LiCaAlF_6$:2% Cr^{3+} derived from the low temperature emission spectrum. The more prominent coupled vibrations correspond to a_{1g}, t_{1u}, e_g and t_{2u}. The ZPL-to-vibration replica intensity ratio is given for each peak; the Huang–Rhys factor of the ith coupled mode of even symmetry was derived through the expression $S_i = I_i/I_{ZPL}$.

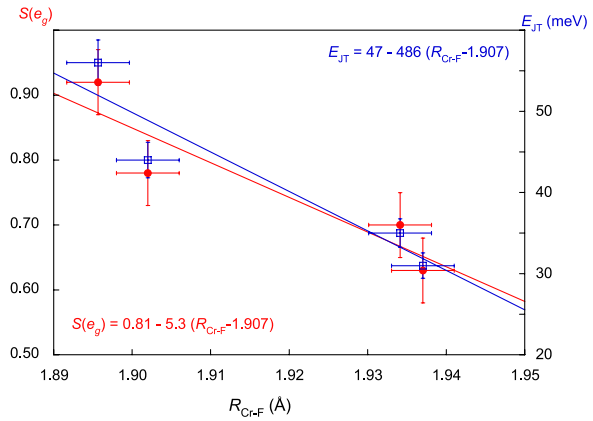

Figure 11. Variation of the Huang–Rhys factor $S(e_g)$ derived from the spin–orbit reduction by the Ham effect and the associated JT energy ($E_{JT} = S_e\hbar\omega_e$) with R_{Cr-F} in the fluoride series collected in table 2.

R_{Cr-F} values are given in table 2. This correlation allows us to conclude that both S_e and E_{JT} increase with $\omega(a_{1g})$ (i.e. decrease with R_{Cr-F}). Aside from S_e and E_{JT}, the ZPL energy (E_{ZPL}) depends linearly on R_{Cr-F} as $E_{ZPL} = 8.28$–$3.4\ R_{Cr-F}$ (in eV and Å, respectively). Figure 10 shows the variation of E_{ZPL} and $\hbar\omega(e_g)$ with R_{Cr-F}. Both variations show linear dependences with R_{Cr-F}, thus indicating that, like the CF splitting, Δ, E_{ZPL} increases upon R_{Cr-F} reduction. On the assumption of an R_{Cr-F} dependence of E_{ZPL} as $E_{ZPL} = K R_{Cr-F}^{-n}$, we obtained $n = 3.7$ from the measured $\frac{\partial E_{ZPL}}{\partial R_{Cr-F}} = -3.4$ eV Å^{-1}. Note that the exponent n is slightly smaller than the calculated one ($n = 4.3$) on the basis *ab initio* calculations for $(CrF_6)^{3-}$ as a function of R_{Cr-F} [20], and also coincides with the measured exponent through high pressure excitation spectroscopy [7, 18]. It must be noted, however, that this value significantly deviates from the value $n = 3.3$ derived from excitation along the fluoroelpasolite series. This unexpectedly small exponent was ascribed to singularities in the first absorption/excitation band due to Fano resonance but this effect is weaker around the ZPL since this spectral region is far apart from such resonances taking place [9].

The variation of $\hbar\omega(e_g)$ with R_{Cr-F} allows us to derive the local Grüneisen parameter associated with the JT mode. From figure 10(a) we obtain $\gamma = \frac{1}{3}\frac{R_{Cr-F}}{\omega(e_g)}(\frac{\partial\omega(e_g)}{\partial R_{Cr-F}}) = 2.9$. This value is significantly higher than γ_{loc} for the totally symmetric mode a_{1g}, thus suggesting that electron–phonon couplings associated with the JT e_g mode should experience stronger variations with R_{Cr-F}. The results of figures 11 and 12 illustrate this behaviour. The variations of the Huang–Rhys parameter $S(e_g)$ (figure 11), derived through the Ham reduction, together with the JT energy $E_{JT} = S(e_g)\hbar\omega(e_g)$ with R_{Cr-F} reveal that both $S(e_g)$ and E_{JT} increase upon R_{Cr-F} reduction. This experimental result is noteworthy since it confirms that, besides a_{1g}, the e_g mode coupling increases with decreasing R_{Cr-F}, making E_{JT} to increase, contrary to expectations based on the reduction of the PL Stokes shift with decreasing R_{Cr-F} [9].

Figure 12 compares the variation of R_{Cr-F} with the corresponding host distance R_{M-F} along the fluoroelpasolite series whose data are collected in table 2. We conclude

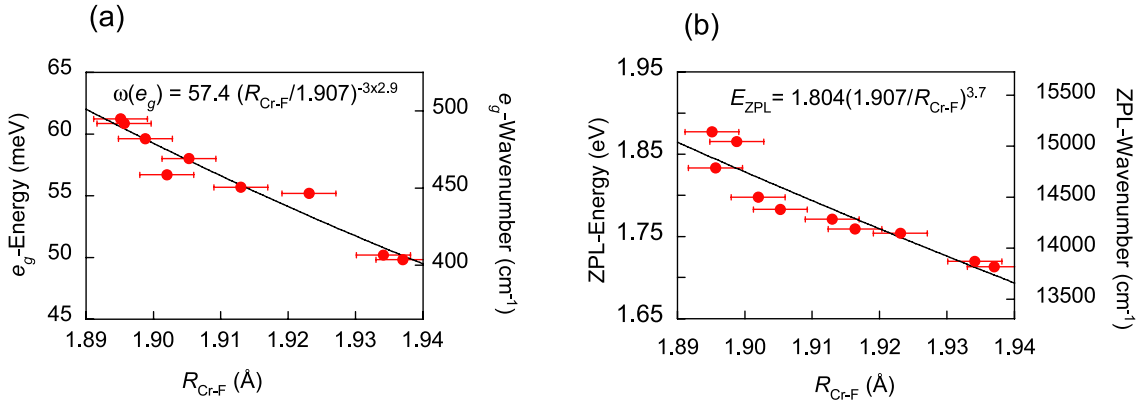

Figure 10. (a) Variation of the vibrational energy of the e_g JT mode with R_{Cr-F} along the fluoride series given in table 2. The curve corresponds to the fit to a Grüneisen equation with $\gamma = 2.9$. The Cr–F distances (R_{Cr-F}) were derived from the a_{1g} vibrational energy through the local Grüneisen parameter of the a_{1g} mode, $\gamma_{loc} = 2.1$ [9]. (b) Variation of the ZPL energy (E_{ZPL}) with R_{Cr-F}. The solid line represents the least-squares fit of the experimental data taken from table 2 to the general equation $E_{ZPL} = K R_{Cr-F}^{-n}$.

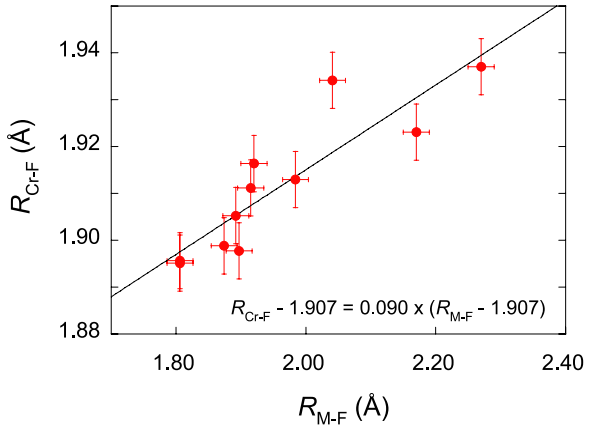

Figure 12. Variation of R_{Cr-F} with the M–F host distance (R_{M-F}). Note the strong outward or inward lattice relaxation around Cr^{3+} (81%), depending on whether R_{M-F} is shorter or longer than $R_{Cr-F} = 1.907$ Å.

that a strong lattice relaxation takes place around the fluorine octahedron when Cr replaces M. Depending on R_{M-F} there is an inward or an outward relaxation of the octahedron if R_{M-F} is longer or shorter than $R_{Cr-F} = 1.907$ Å, respectively, the relaxation being about 90% of the distance difference $R_{M-F} - 1.907$. It means that R_{Cr-F} varies within 0.05 Å around 1.907 Å even if the host distance R_{M-F} varies 0.5 Å along the series (figure 12).

3.4. Thermal shifts: explicit and implicit contributions

Figure 2 shows the variation of the emission and absorption bands of $LiCaAlF_6:Cr^{3+}$ in the 19–300 K range. It is important to note that both absorption and emission bands shift to lower energies upon increasing temperature, whereas a thermal blueshift is observed in the first absorption and emission peaks associated with the ($^4T_1 \rightarrow {}^6A_1$) transition of Mn^{2+} in MnX_6^{4-} (X: Cl, F) [32, 33]. This opposite thermal shift behaviour between Cr^{3+} ($3d^3$) and Mn^{2+} ($3d^5$) has often been attributed to the different CF dependence of the absorption (or emission) energy with the crystal volume due to thermal expansion effects. However, this analysis is not complete since thermal shifts also contain contributions arising from changes of the thermal population in vibronic states.

In a general way, the energy variation with temperature can be written as

$$\left(\frac{\partial E}{\partial T}\right)_P = \left(\frac{\partial E}{\partial T}\right)_V + \left(\frac{\partial E}{\partial V}\right)_T \left(\frac{\partial V}{\partial T}\right)_P.$$

The first term represents the explicit thermal contribution, i.e. the energy variation with temperature for a constant volume, and the second term, the implicit thermal contribution, which represents the shifts due to volume variations by thermal expansion effects [32]. The different thermal shift behaviour of Cr^{3+} and Mn^{2+} is related to the distinct dependence of their excitation energy on the CF strength (Δ) or the crystal volume (V): $\partial E(^4T_2)/\partial V \approx \partial\Delta/\partial V < 0$ for Cr^{3+}, whereas $\partial E(^4T_1)/\partial V \approx -(\partial\Delta/\partial V) > 0$ for Mn^{2+} as can be derived from the sign of the $\partial E(^4T_i)/\partial\Delta$ slope in the respective Tanabe–Sugano diagrams which are opposite for d^3 and d^5 ions [34]. Interestingly, the slope sign explains the different thermal shift behaviour found in Cr^{3+} and Mn^{2+} not only for the implicit contribution but also for the explicit one. In fact, a positive (or a negative) sign of $\partial E(^4T_i)/\partial V$ implies a volume increase (or reduction) on passing from the electronic ground state to the excited state. This means that the coupled vibrational modes with positive Grüneisen parameters [32] will decrease (or increase) their frequency in the corresponding ^4T_i excited state of Cr^{3+} (or Mn^{2+}). Therefore explicit redshifts (or blueshifts) are expected with increasing temperature whether the vibrational frequencies in the excited state are lower (or higher) than in the ground state [32]. Thus, both implicit and explicit thermal shifts have the same sign, and mainly rely on the volume dependence of the excited state energy. This result allows us to understand why thermal shifts have very often been interpreted on the basis of thermal expansion effects alone, ignoring possible explicit effects. The relative contribution of these two effects can be solved experimentally if both the thermal expansion coefficient and pressure shifts are known for a given compound.

The energy variation with temperature, $E(T)$, shown in figure 2 is in agreement with the proposed model. The larger redshifts observed in absorption than in emission reflect an additional explicit contribution due to the ED mechanism assisted by odd-parity vibrations of ω_u frequency [32]. This extra contribution separates emission and absorption bands and thus increases the Stokes shift by about $2\hbar\omega_u$ from high to low temperature. Both the absorption and emission bands experience additional shifts of $-\hbar\omega_u$ and $+\hbar\omega_u$ from low to high temperature, thus making the absorption thermal redshift larger than the emission one, as experimentally observed.

X-ray diffraction experiments as a function of pressure and temperature [35] together with high pressure spectroscopic data [7] performed in $LiCaAlF_6:Cr^{3+}$ allow us to get quantitative estimates of the explicit and implicit contributions to the thermal shifts.

From the linear expansion coefficients of $LiCaAlF_6$ $\alpha(\| c) = 3.6 \times 10^{-6}$ K^{-1} and $\alpha(\perp c) = 22 \times 10^{-6}$ K^{-1} (volume expansion coefficient, $\alpha = 48 \times 10^{-6}$ K^{-1}) [35]; its bulk modulus $B_0 = 93$ GPa [8] and the pressure dependence of the absorption and emission bands $\frac{\partial E}{\partial P} = 11$ meV GPa^{-1} for both bands [7, 18], we obtained a contribution to the implicit thermal shift as

$$\left(\frac{\partial E}{\partial T}\right)_{\text{implicit}} = \left(\frac{\partial E}{\partial V}\right)_T \left(\frac{\partial V}{\partial T}\right)_P = \left(\frac{\partial E}{\partial P}\right)_T \left(\frac{\partial P}{\partial V}\right)\left(\frac{\partial V}{\partial T}\right)_P$$
$$= \frac{B_0}{V_0} V_0 \alpha \left(\frac{\partial E}{\partial P}\right)_T = B_0 \alpha \left(\frac{\partial E}{\partial P}\right)_T$$
$$\left(\frac{\partial E}{\partial T}\right)_{\text{implicit}} = B_0 \alpha \left(\frac{\partial E}{\partial P}\right)_T = 93 \times 4.8 \times 10^{-5}$$
$$\times 11 \times 10^{-3} = 4.9 \times 10^{-5} \text{ eV K}^{-1}.$$

This value must be compared with the experimental thermal shift $\left(\frac{\partial E}{\partial T}\right)_P$ at 300 K. From figure 2, we derived $\left(\frac{\partial E}{\partial T}\right)_P = 12 \times 10^{-5}$ eV K^{-1} for both emission and absorption bands. This means that the implicit contribution represents 40% of the total shift while the remaining 60% is due to the explicit contribution. A similar result was obtained

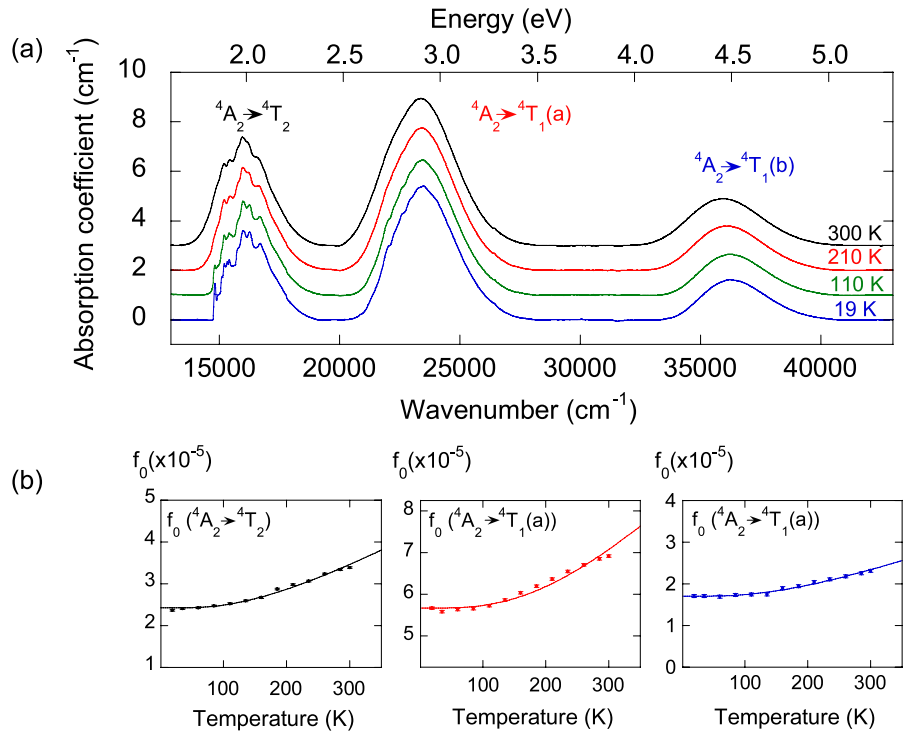

Figure 13. Optical absorption spectra of $LiCaAlF_6$:2% Cr^{3+} in the 19–300 K range. (b) Temperature variation of the first-order moment $M_0(T)$ or the oscillator strength $f(T)$ (equations (4) and (5)) of each absorption band. The obtained fitting parameters are given in table 4.

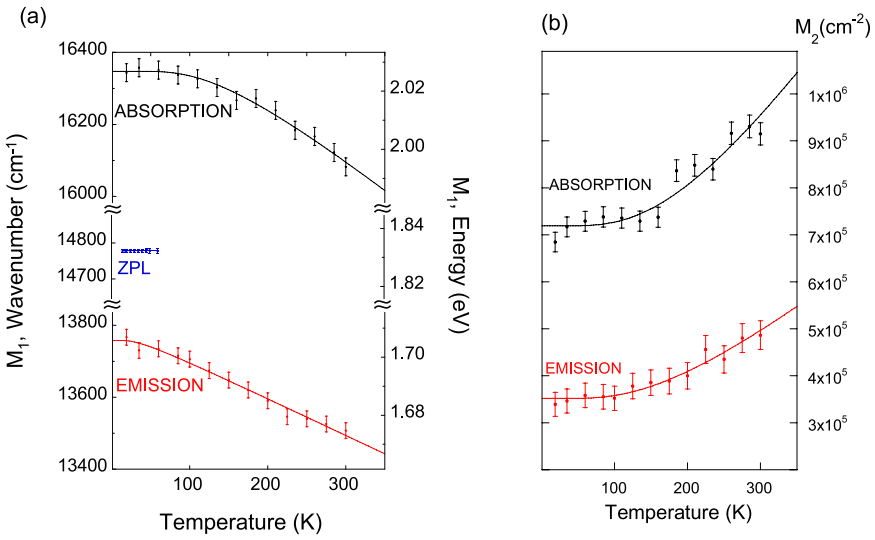

Figure 14. (a) Temperature dependence of the energy (first-order moment, $M_1(T)$) corresponding to the emission and first absorption bands. The variation of the ZPL energy in the temperature range of detection is included. (b) Temperature dependence of the second-order moment $M_2(T)$ associated with bandwidths of the $^4A_2 \leftrightarrow {}^4T_2$ absorption and emission bands in $LiCaAlF_6$:2% Cr^{3+}. The fitting parameters are given in table 5.

for Mn^{2+}-fluoroperovskites ABF_3:Mn^{2+} [32], suggesting that both terms contribute significantly to the thermal shift although the explicit contribution is slightly higher than the implicit one. This contrasts with the behaviour of weakly coupled systems as a trapped exciton in semiconductors like silicon, where the thermal shift of the trapped exciton ZPL is fully governed by the explicit contribution [36]. As a general conclusion, present results suggest that the stronger the electron–phonon coupling is, the larger the volume expansion contribution to the thermal shift.

3.5. Variation of the bandwidth and oscillator strength with temperature

In intermediate electron–phonon coupled systems like $LiCaAlF_6$:Cr^{3+} (Huang–Rhys factors: $S_e = S_a \approx 1$), the peak broadening and oscillator strength enhancement with

Table 4. Coupled mode energy and fitting parameters f_{0i} for the measured intensity of the absorption bands $M_0(T)$ to equation (4) in terms of the oscillator strength $f_0(T) = \sum_i f_{0i} \coth \frac{\hbar\omega_{ui}}{2k_BT}$.

Coupled mode energy	$f_{0i} \times 10^{-5}$	$^4A_2 \rightarrow {}^4T_2$	$^4A_2 \rightarrow {}^4T_1$ (a)	$^4A_2 \rightarrow {}^4T_1$ (b)
$\hbar\omega(t_{2u}) = 28.8$ meV	$f_{01} \times 10^{-5}$	1.1	0.77	0.41
$\hbar\omega(t_{1u}(b)) = 38.6$ meV	$f_{02} \times 10^{-5}$	—	—	—
$\hbar\omega$ (t_{1u}(s) and τ_{stat}^{-1}) = 72.0 meV	$f_{03} \times 10^{-5}$	1.4	4.9	1.2

Table 5. Huang–Rhys parameter S_i for emission and absorption bands obtained by fitting the measured bandwidth $M_2(T)$, to $M_2(T) = \sum_i S_i(\hbar\omega_i)^2 \coth \frac{\hbar\omega_i}{2k_BT}$ (equation (3)).

		Emission	Absorption $^4A_2 \rightarrow$		
Coupled mode energy	S_i	$^4T_2 \rightarrow {}^4A_2$	$^4T_2$	$^4T_1$(a)	$^4T_1$(b)
$\hbar\omega(e_g) = 60.9$ meV	$S_1 = S(e_g)$	0.9 ± 0.2	2.4 ± 0.2	6.2 ± 0.2	4.23 ± 0.2
$\hbar\omega(t_{2g}) = 32.2$ meV	$S_2 = S(t_{2g})$	1.8 ± 0.2	2.1 ± 0.2	—	6.7 ± 0.2

temperature are shown by the increase of the bandwidth $H(T)$ and the integrated band intensity $I(T)$ (figures 13 and 14). Their thermal dependence is reasonably well described by

$$M_2(T) = \sum_i S_i(\hbar\omega_i)^2 \coth \frac{\hbar\omega_i}{2k_BT} \tag{3}$$

$$M_0(T) = \sum_i f_{0i} \coth \frac{\hbar\omega_{ui}}{2k_BT} \tag{4}$$

where $M_0(T)$ and $M_2(T)$ are the zero- and second-order moment of the band, respectively. For Gaussian profiles M_2 is related to the full width at half-maximum (FWHM) through $\mathrm{FWHM}(T) = H(T) = (8\ln 2)^{1/2}\sqrt{M_2(T)}$. ω_i is the angular frequency of the ith coupled mode of even parity, ω_{ui} the odd-parity frequency of the ith enabling mode and f_{0i} is the oscillator strength contribution due to zero-point motion by the ith enabling mode ($T = 0$ K). The zero-order moment $M_0(T)$ is related to the integrated absorption coefficient by $M_0(T) = \int_{\mathrm{band}} k(T)\,\mathrm{d}E$ (in cm^{-1} and eV units, respectively). $M_0(T)$ is proportional to the oscillator strength $f(T)$ through the equation

$$f(T) = 8.20 \times 10^{16} \frac{n}{(n^2+2)^2} \frac{M_0(T)}{N} \tag{5}$$

$n = 1.92$ is the refractive index [35], $N = [Cr^{3+}] = 1.9 \times 10^{20}$ cm^{-3}. The measured oscillator strength and bandwidth and their fitted curves to equations (3)–(5) are shown in figures 13 and 14. Tables 4 and 5 collect the corresponding fitted parameters. Through these fits we are able to establish which $(CrF_6)^{3-}$ modes are coupled in each case. The oscillator strength $f(T)$ increases with temperature with the same dependence as equation (4), t_{2u} ($\hbar\omega_u = 28.8$ meV) being the main enabling mode governing $f(T)$. Although the highest energy mode t_{1u}(b), significantly contributes to $f(T)$, its contribution in the 19–300 K range can be considered as a constant term. Therefore this contribution may come either from an ED transition induced by t_{1u}(b) or from MD contributions which are practically temperature-independent. The latter possibility must be ruled out after the vibronic analysis of the emission and absorption spectra. In fact, the phonon side band is built from pure MD ZPL origins and from some ED false origins displaced $\hbar\omega_u$ from the ZPL (table 4). This is supported by the fact that the ED false origins and ZPL have almost the same intensity (table 4). This result is confirmed by previous findings on $(MnF_6)^{4-}$ systems [32]. Based on lifetime measurements, $\tau(T)$, it is concluded that the octahedral t_{2u} mode governs the ED vibronic mechanism in centro-symmetric Mn^{2+} systems.

The temperature dependence of the bandwidth is mainly governed by the JT mode e_g and by the t_{2g} mode (table 5) as is derived by the $M_2(T)$ fit to equation (3) for the emission band (figures 2 and 14). Note that the Huang–Rhys factor associated with the e_g mode derived from $M_2(T)$ is $S_e = 0.9$ in good agreement with $S_e = 0.92$ obtained from ZPL splitting reduction and thus confirms the mode analysis that has been performed. In general, the Huang–Rhys parameters derived through $M_2(T)$ from absorption bands substantially differ from the emission value. Such a discrepancy is probably due to the complex absorption band structure consisting of at least two different interacting transitions (Fano resonance) making it the analysis of $H(T)$ or $M_2(T)$ in terms of one-single transition band meaningless. Additional broadening from multiple transitions should be considered in the analysis of $M_2(T)$ in absorption. Therefore a proper comparison between the Huang–Rhys factor S_e derived from different methods should be suitably done on the basis of the temperature dependence of the emission band rather than absorption bands.

4. Conclusions

The main PL properties of $LiCaAlF_6:Cr^{3+}$ are explained on the basis of a single Cr^{3+} centre of nearly-octahedral D_{3d} symmetry. The ZPL energy and the vibrational structure related to the internal modes of $(CrF_6)^{3-}$ are consistent with a short Cr–F distance attained in $LiCaAlF_6:Cr^{3+}$ ($R_{Cr-F} = 1.894$ Å) in comparison with other fluorides. The ZPL splitting reflects a dynamical JT effect in the $^4T_2$ state that reduces the spin–orbit interaction by a factor $\gamma = 0.25$, which is, together with $\gamma = 0.14$, found in $K_2NaScF_6:Cr^{3+}$, the largest reductions among $(CrF_6)^{3-}$ systems. The so-obtained Huang–Rhys factor of the e_g mode ($S_e = 0.92$) is in agreement with the ratio of the intensity of its one-phonon replica and the ZPL.

The temperature dependence of the oscillator strength $f(T)$, the transition energy $E(T)$ and the bandwidth FWHM(T) reveals that (1) t_{2u} is the most efficient odd-parity mode to enable the $^4A_2 \rightarrow {}^4T_2$ transition by increasing its ED oscillator strength; (2) thermal broadenings are mainly governed by even-parity modes t_{2g} and e_g with minor contribution of the totally symmetric a_{1g} mode and (3) both emission and absorption bands shift to lower energy with increasing temperature, the emission shift being larger than the corresponding absorption one. These asymmetric thermal shifts are due to the coupling to the transition-enabling odd-parity modes, which induce opposite shifts in emission and absorption. Interestingly, we were able to separate the implicit and explicit contributions to the thermal shifts thanks to available high pressure spectroscopic data for $LiCaAlF_6:Cr^{3+}$. We show that the thermal expansion (implicit contribution) represents 40% of the total shift whereas the remaining 60% is induced by changes in the thermal population caused by the different vibrational frequencies attained in the ground and excited states (explicit contribution). Finally, we demonstrate that both the Huang–Rhys factor S_e and the associated JT energy of the e_g mode increase upon R_{Cr-F} reduction.

Acknowledgments

Financial support from the Spanish Ministerio de Ciencia e Innovación (project no. MAT2008-06873-C02-01/MAT) is acknowledged. FR also wishes to offer his thanks for partial support from the Research Intensification program (I3) of the University of Cantabria, and MNS-O thanks the MEC for an FPU grant (ref. AP-2004-5954). This work has been carried out within the framework of the MALTA CONSOLIDER Ingenio 2010 program (ref. CSD2007-00045).

References

[1] Payne S A, Chase L L and Wilke G D 1989 *J. Lumin.* **44** 167–76
[2] Smith L K, Payne S A, Kway W L, Chase L L and Chai B H T 1992 *IEEE J. Quantum Electron.* **28** 2612–8
[3] Dolan J F, Kappers L A and Bartram R H 1986 *Phys. Rev.* B **33** 7339
[4] Hömmerich U and Bray K L 1995 *Phys. Rev.* B **51** 12133
[5] Kaminska A, Suchocki A, Arizmendi L, Callejo D, Jaque F and Grinberg M 2000 *Phys. Rev.* B **62** 10802
[6] Grinberg M, Barzowska J, Shen Y and Bray K L 2001 *Phys. Rev.* B **63** 214104
[7] Sanz-Ortiz M N, Rodriguez F, Hernandez I, Valiente R and Kück S 2006 *High Pressure Res.* **26** 345–8
[8] Grzechnik A, Dmitriev V, Weber H-P, Gesland J-Y and Van Smaalen S 2004 *J. Phys.: Condens. Matter* **16** 1033
[9] Hernandez I, Rodriguez F and Tressaud A 2008 *Inorg. Chem.* **47** 10288–98
[10] Tanner P A 2004 *Chem. Phys. Lett.* **388** 488–93
[11] Marco De Lucas M C, Dance J M, Rodriguez F, Tressaud A, Moreno M and Grannec J 1995 *Radiat. Eff. Defects Solids* **135** 517–20
[12] Wein G R *et al* 2001 *J. Phys.: Condens. Matter* **13** 2363
[13] Greenough P and Paulusz a G 1979 *J. Chem. Phys.* **70** 1967–72
[14] Sosman L, Da Fonseca R, Tavares A, Nakaema M and Bordallo H 2006 *J. Fluoresc.* **16** 317–23
[15] Avram C N, Brik M G and Avram N M 2008 *J. Lumin.* **128** 982–4
[16] Hernández I and Rodríguez F 2003 *Phys. Rev.* B **67** 012101
[17] Hernández I, Rodríguez F and Hochheimer H D 2007 *Phys. Rev. Lett.* **99** 027403
[18] Sanz-Ortiz M N, Rodríguez F, Hernández I, Valiente R and Kück S 2010 *Phys. Rev.* B **81** 045114
[19] Woods A M, Sinkovits R S, Charpie J C, Huang W L, Bartram R H and Rossi A R 1993 *J. Phys. Chem. Solids* **54** 543–52
[20] Brik M G and Ogasawara K 2006 *Phys. Rev.* B **74** 045105
[21] Wenger O S and Güdel H U 2001 *J. Chem. Phys.* **114** 5832–41
[22] Rodriguez F, Riesen H and Güdel H U 1991 *J. Lumin.* **50** 101–10
[23] Avram C N and Brik M G 2003 *J. Lumin.* **102/103** 81–4
[24] Flerov I N, Gorev M V, Aleksandrov K S, Tressaud A, Grannec J and Couzi M 1998 *Mater. Sci. Eng.* R **24** 81–151
[25] Tressaud A, Khairoun S, Chaminade J P and Grannec J 1987 *J. Fluor. Chem.* **35** 174
[26] Brik M G, Avram N M and Tanaka I 2004 *Phys. Status Solidi* b **241** 2982–93
[27] Zuniga F J, Tressaud A and Darriet J 2006 *J. Solid State Chem.* **179** 3607–14
[28] Güdel H U and Snellgrove T R 1978 *Inorg. Chem.* **17** 1617–20
[29] Ham F S 1968 *Phys. Rev.* **166** 307
[30] Jahn H A and Teller E 1937 *Proc. R. Soc.* A **161** 220–35
[31] Sturge M D 1967 *Solid State Physics* (New York: Academic)
[32] Marco De Lucas M C, Rodriguez F and Moreno M 1995 *J. Phys.: Condens. Matter* **7** 7535–48
[33] Marco de Lucas M C, Rodríguez F, Güdel H U and Furer N 1994 *J. Lumin.* **60** 581–4
[34] Sugano S, Tanabe Y and Kamimura H 1970 *Multiplets of Transition-Metal Ions in Crystals* (New York: Academic)
[35] Woods B W, Payne S A, Marion J E, Hughes R S and Davis L E 1991 *J. Opt. Soc. Am.* B **8** 970–7
[36] Rodriguez F, Davies G and Lightowlers E C 2000 *Phys. Rev.* B **62** 6180–91
[37] Sabelli C 1987 *Neues Jahrb. Mineral.-Mon.hefte* **11** 481–7
[38] Mortier M, Wang Q, Buzare J Y, Rousseau M and Piriou B 1997 *Phys. Rev.* B **56** 3022–31
[39] Reber C, Güdel H U, Meyer G, Schleid T and Daul C A 1989 *Inorg. Chem.* **28** 3249–58
[40] Siebert G and Hoppe R 1972 *Z. Anorg. Allg. Chem.* **391** 117
[41] Doriguetto a C, Boschi T M, Pizani P S, Mascarenhas Y P and Ellena J 2004 *J. Chem. Phys.* **121** 3184–90
[42] Vedrine A, Besse J P, Baud G and Capestan M 1970 *Rev. Chim. Miner.* **7** 593